

Elastic turbulence in a curvilinear channel flow

Yonggun Jun and Victor Steinberg

Department of Physics of Complex Systems, Weizmann Institute of Science, Rehovot, 76100 Israel

(Dated: August 22, 2011)

We report detailed quantitative studies of elastic turbulence in a curvilinear channel flow in a dilute polymer solution of high molecular weight polyacrylamide in a high viscosity water-sugar solvent. Detailed studies of the average and rms velocity and velocity gradients profiles reveal an emergence of the boundary layer associated with the nonuniform distribution of the elastic stresses across the channel. The characteristic boundary width is independent of the Weissenberg number Wi and proportional to the channel width that follows from our early investigations of the boundary layer in elastic turbulence of different flow geometries. The appearance of the characteristic spatial scales of the order of the boundary layer width of both velocity and velocity gradient in the correlation functions of the velocity and velocity gradient fields in a bulk flow suggests that rare and strong parcels of excessive elastic stresses, concentrated in the boundary layer, are ejected into the bulk flow similar to jets observed in passive scalar mixing. And finally, the experimental results show that one of the main predictions of the theory of elastic turbulence, namely the saturation of the normalized rms velocity gradient in the bulk flow of elastic turbulence contradicts to the experimental observations both qualitatively and quantitatively in spite of the fact that the theory explains well the observed sharp decay of the velocity power spectrum. The experimental findings call for further development of theory of elastic turbulence in a bounded container, similar to what was done for a passive scalar problem.

PACS numbers: 47.20.Gv, 47.50.-d, 47.27.-i

I. INTRODUCTION

The addition of small amount of long polymer molecules into a fluid makes it elastic and capable to storing elastic stresses that may strongly alter flow properties [1]. First of all, the elastic stresses generated by the polymer stretching in the flow becomes the main source of nonlinearity in the polymer solution flow at low Reynolds numbers Re . As the result, an elastic instability shows up, when the elastic energy overcomes the dissipation due to polymer relaxation. The ratio of the nonlinear elastic term to the linear relaxation is defined by the Weissenberg number Wi [1], which is the main control parameter in the problem, and the elastic instability occurs in a shear flow with curvilinear trajectories at $Wi_c \geq 1$. Above the purely elastic instability, a path to a chaotic flow in a form of irregular flow patterns at $Wi > Wi_c$ was studied in three flow geometries: Couette flow between cylinders, swirling flow between two disks, and flow in a curvilinear channel [2, 3]. Further increase of Wi at vanishingly small Re leads to the most remarkable phenomenon discovered recently experimentally [2] and then studied during the last decade in the increasing number of experimental [3–8] and theoretical [9–12] papers, namely "elastic turbulence". It is a spatially smooth and random in time flow, which is driven by strong polymer stretching and resulting elasticity observed at sufficiently large Wi and at vanishingly small Re . Many properties of the elastic turbulence regime, namely statistics of velocity and velocity gradient fields, spatial and temporal velocity correlation functions and power-law behavior of velocity power spectrum, a new length scale—the boundary layer width and its properties, scaling and statistical properties of torque and pressure

fluctuations, in a von Karman swirling flow between two disks were observed and investigated experimentally and only a few of them theoretically and numerically [7].

On the other hand, a detailed description of similar properties in a channel flow is lacking, though elastic turbulence in a curvilinear channel was used to demonstrate its effectiveness in mixing in macro- as well as in micro-channels [3–5, 13, 14]. In a 3 mm wide curvilinear channel the longitudinal and transverse flow velocity components were measured by a laser Doppler anemometer at the bend $N = 12$ near the middle of the half-ring in the middle of the channel at a fixed value of Wi , about twice above the onset to the elastic instability. The power spectra of the longitudinal and transversal velocity components show a broad region of an algebraic decay $f^{-3.3}$ in the frequency domain. The rms velocity of fluctuations was $0.09\langle V \rangle$ and $0.04\langle V \rangle$ for the longitudinal and transverse components, respectively, where $\langle V \rangle$ is the mean longitudinal velocity component. Since the power spectra were measured at a point with more than 10 times higher mean than the characteristic fluctuation velocity, the Taylor hypothesis can be used to transfer the power-law-decay in the frequency domain to the wave number k domain as $k^{-3.3}$, which is very close to the scaling exponent found in the von Karman swirling flow between two disks in both frequency and wave number domains [2, 7]. Another measurements of the flow velocity were carried out in the micro-channel of a similar design as the 3 mm channel but scaled down 30 times compared with the macro-channel version [5, 13]. In order to define the onset of the elastic instability, the both longitudinal and transverse velocity field components were measured by microscopic particle image velocimetry, micro-PIV, as a function of the pressure drop Δp along the channel. The

resulting flow resistance, defined as $\Delta p/\bar{V}$, as a function of the pressure drop shows sharp but continuous change in the dependence that determines the instability onset. Similar effect is observed on the plot of V_θ^{rms} as well as V_r^{rms} versus Δp [5, 13]. Temporal dependence of the longitudinal velocity as well as its correlation function were also measured together with the velocity correlation time. By using $0.2\ \mu\text{m}$ fluorescent particles streamwise vortices were visualized by means of horizontal confocal scanning microscopy in the middle plane of the channel [5, 13]. In the recent detailed studies of mixing in a curvilinear channel of $1\ \text{mm}^2$ cross-section using elastic turbulence, some partial characterization of the velocity field necessary for quantitative characterization of mixing, namely both average radial $\langle V_r \rangle$ and longitudinal $\langle V_\theta \rangle$ velocity profiles across the channel, dependence of $\langle V_\theta \rangle$ on Wi , profiles of rms of longitudinal $\partial V_\theta/\partial r$ and radial $\partial V_r/\partial r$ velocity gradients, was carried out [14].

The first and currently the only theory of elastic turbulence was developed right away after the first publication of its discovery. The main concern of the theory was to explain the key experimental observation in elastic turbulence, namely the sharp algebraic decay of the velocity power spectrum with the scaling exponent δ between -3.3 and -3.6 [2, 3]. Due to the sharp velocity spectrum decay, the velocity and velocity gradient are both determined mostly by the integral scale, i.e., the vessel size. It means that elastic turbulence is essentially a spatially smooth and random in time flow, dominated by strong nonlinear interaction of a few large-scale modes. It is the same random flow that occurs in hydrodynamic turbulence below the dissipation scale and called Batchelor flow regime [16]. It is resulted from stretching and folding of elastic stress field, similar to a passive scalar stretching and folding in the Batchelor regime of mixing. A crucial difference between elastic turbulence and passive scalar mixing is that in the case of elastic turbulence the corresponding elastic stress field is not passive but reacts back on the driving velocity field and in such way stabilizes the flow [9, 17]. There are two aspects of theory of polymer stretching in a flow. First is a description of statistics of polymer stretching and a coil-stretch transition in a spatially smooth and random in time flow, and second is a characterization of the properties of elastic turbulence resulting from the polymer stretching.

The first aspect requires a microscopic approach to the problem, which provides a quantitative prediction on the coil-stretch transition of a polymer and on a saturation of the polymer stretching in a spatially isotropic random unbounded flow and a detailed prescription to experimentally verify it [18, 19]. This prediction was tested experimentally, and good agreement was found [20, 21]. The coil-stretch transition has remarkable macroscopic consequence on a flow: properties of the polymer solution become essentially non-Newtonian and the stretched polymers significantly alter the flow due to their back reaction. The second aspect, on the other hand, requires a macroscopic description of elastic turbulence, which has

been developed by Lebedev et al [9, 17] and is based on polymers with linear elasticity and the feedback reaction on the flow. The theory of elastic turbulence uses the set of equations for the elastic stress tensor and velocity fields. Hydrodynamic description of a polymer solution flow and of dynamics of elastic stresses for linear polymers is analogous to that of a small-scale fast dynamo in magneto-hydrodynamics (MHD) and also of turbulent advection of a passive scalar in the Batchelor regime [9, 16], though some significant differences exist. The stretching of the magnetic lines is similar to the polymer stretching, and the difference with MHD lies in the relaxation term that replaces the diffusion term in MHD description, whereas in the passive scalar advection problem the dynamo effect, i.e. feedback reaction on the flow, is absent. In all three cases the basic physics is the same, rather general and directly related to the classical Batchelor regime of mixing: stretching and folding of the passive scalar, magnetic, or stress fields by a random advecting flow in all three cases.

Theory of elastic turbulence in an unbounded flow of a polymer solution is based on the following assumptions [9, 17]. (i) A statistically stationary state occurs due to the feedback reaction of stretched polymers (or the elastic stress) on the velocity field that leads to a saturation of the elastic stress σ_p and rms of the velocity gradients $(\partial V_i/\partial x_j)_{rms}$ (and so $Wi_{loc} = (\partial V_i/\partial x_j)_{rms}\lambda$, where λ is the longest polymer relaxation time) even for polymers with linear elasticity [9, 17]. The saturation value in a bulk of elastic turbulence is $Wi_{loc} \simeq 1$ and constant at all Wi above the coil-stretch transition. It is the key theoretical prediction [9, 17]. (ii) Both dissipative terms due to viscosity and polymer relaxation, which appear in the equation for the dissipation of elastic energy [17], are of the same order, i.e. $\sigma_p/\lambda \sim \eta(\nabla V)^2$ or otherwise $\sigma_p\lambda/\eta \sim Wi_{loc}^2$, where η is the viscosity. Then both assumptions lead to the following result: the normalized elastic stress $\sigma_p\lambda/\eta \simeq 1$ and also saturates. These two important theoretical predictions deserve a stringent experimental test. Indeed, the value of elastic stresses was measured in the recent experiment in microscopic arrangement of a swirling flow [15] and strong discrepancy was identified. The first prediction on the saturation of Wi_{loc} in a bulk flow of elastic turbulence was examined in a swirling macroscopic flow [7] and quantitative disagreement was found. On the other hand, the further theoretical analysis leads to a power-like decaying spectrum for the elastic stresses and for the velocity field fluctuations with the exponent $|\delta| > 3$ in a good accord with the experimental results [2, 3]. The close value of the exponent in the velocity power spectra decay was also obtained in the numerical simulations of elastic turbulence based on the Kolmogorov shear flow of a dilute polymer solution described by the Oldroyd-B model [10, 11].

In this paper we provide a complete characterization of the channel flow in the elastic turbulence regime, present statistics, correlations and scaling of velocity and velocity gradient fields in the bulk as well as in the vicinity

of the wall, and also properties of the velocity gradient boundary layer that provide us the possibility also to further test the theoretical prediction about the saturation of Wi_{loc} .

The paper is organized as follows. In Sec. II, the experimental setup is described in details. In Sec. III the experimental results are presented. Here we first describe in Sec. IIIA flow structure and experimental determination of the elastic instability threshold. Then in Sec. IIIB various velocity and velocity gradient profiles at determination of the boundary layer widths of velocity and velocity gradient and its functional dependence are described. Temporal and spatial correlation functions of velocity and velocity gradients and correlation times at lengths as a function of Wi are presented in Sec. IIIC. And finally, statistics of velocity and velocity gradient and structure function scalings are discussed in Sec. IIID. Discussion of the experimental results is given in Sec. I and conclusions are presented in Sec. V.

II. EXPERIMENTAL SET-UP AND PROCEDURE

The experiments were conducted in a curvilinear channel of about 1 mm^2 square cross-section machined out of plexiglass (lucite). The width size was chosen to reduce by an order of magnitude the amount of a working fluid (polymer solution) used in the first experiment with channel width of 3 mm [3, 4] and to increase spatial resolution of a velocity field in peripheral regions compared with the second experiment, where a micro-channel of $100 \mu\text{m}^2$ square cross-section was used [5, 13]. The channel used in the current experiment contained 63 pairs of identical smoothly connected half-rings (bends or units) with inner and outer radii of $R_i = 1 \text{ mm}$ and $R_o = 2 \text{ mm}$, respectively, and sufficiently high gap ratio $d/R_i = 1$, the same as in the previous experiments [14], which was intended to facilitate the onset of the elastic instability at sufficiently low Wi . Here $d = R_o - R_i$ is the channel width. The precise dimensions of the channel were 0.95 mm width at the midplane of the channel, where measurements of mixing were performed (with $\pm 0.05 \mu\text{m}$ differences in the width at the top and bottom of the channel), and 1.025 mm depth. Thus the entire channel length was approximately 59.4 cm measured along a channel midplane (see Fig. 1). The channel main body and the lid sealed with O-ring were squeezed between two stainless steel plates to seal the channel against leaks and to preserve a flatness along the channel.

The pulse Nd-YAG laser of the 532 nm wavelength (New Wave Research Ltd.), which produces pulses of power $30 \text{ mJ}/5\text{ns}$ with time delay between the pulses of $10 \mu\text{s}$, was used to conduct particle image velocimetry (PIV) measurements. Time differences between two consecutive images was chosen depending on Wi between 0.51 and 1.84 msec , and it was synchronized between laser pulses and camera via the control units of the PIV

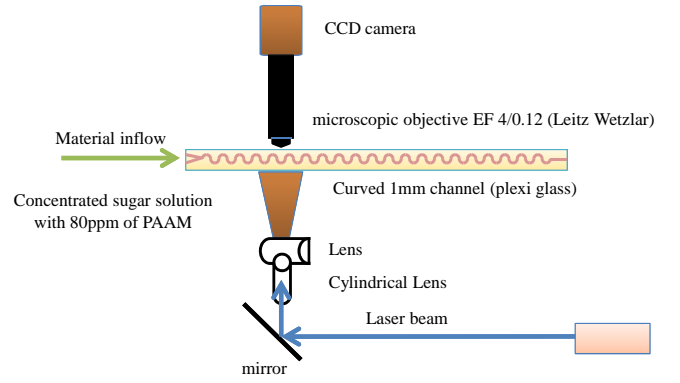


Figure 1: The schematic drawing of the experimental setup

laser system. For visualization of velocity field measurements, red fluorescent particles (Duke Scientific Ltd.) of $2 \mu\text{m}$ at concentration of 150 ppm were used. As in the previous setups [3, 4, 14], the channel was illuminated from a side by laser beam transformed by an appropriate optical setup containing two cylindrical lenses to a broad light sheet of a thickness about $\sim 50 \mu\text{m}$ in the observation region (see Fig. 1). Thinner light sheet causes a permanent damage to plexiglass. The laser beam sheet produced a thin cut in the 3D flow, parallel to the top and bottom of the channel at its midplane. Fluorescent light emitted by the particles in the direction perpendicular to the beam plane was detected by a charge coupled device (CCD) via a microscope objective EF 4.0/0.12 (Leitz Wetzlar) mounted on the plastic tube (guide). The CCD camera Grasshopper, model Gras-1455M-C (Grey Point Research) of 16 bits grey scale resolution and with spatial resolution of 1280×768 pixels at up to 30 frames/sec rate was used. Together with the microscope objective, it provided a PIV spatial resolution of $0.576 \mu\text{m}/\text{pixel}$. The size of the PIV image was 1280×384 pixels. The window size to get velocity vectors was taken 32×8 pixels that corresponded to $18.4 \times 4.6 \mu\text{m}^2$. Total 130 velocity vectors in the transverse direction to the flow were obtained from PIV. Thus the velocity gradients were calculated on $dr = 4.6 \mu\text{m}$. The images were taken at the rate 10 fps . Since each two consecutive images were transformed into one velocity field, the final rate was 5 Hz of the velocity field sampling. Total 1000 velocity field were used for averaging.

The velocity profile in the channel flow of the Newtonian solvent measured by PIV has been used for calibration. Figure 2 presents the results of longitudinal velocity profiles $V_\theta(r/d)$ across the channel in a laminar flow of the solvent for various pressure drops. (We use in the channel middle plane as the coordinates z and r , as longitudinal and transversal to the channel walls, respectively, and V_θ and V_r as the longitudinal and radial components of the velocity field, respectively.) We visualize just a part of the channel cross-section to increase a spatial resolution, since we later on use only the velocity maximum values and the velocities in a peripheral region close to

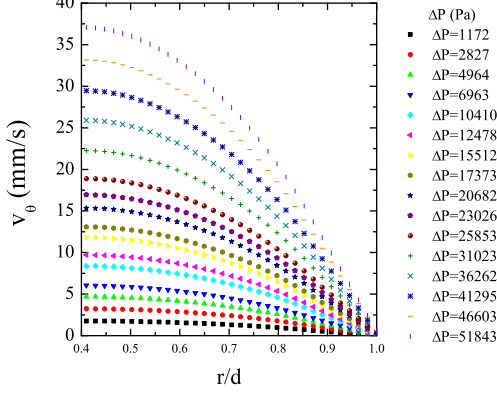


Figure 2: Longitudinal velocity profiles across a channel of a solvent laminar flow in a curvilinear channel at various pressure drops (starting from small values at bottom to top; $r = 0$ corresponds to the inner channel wall).

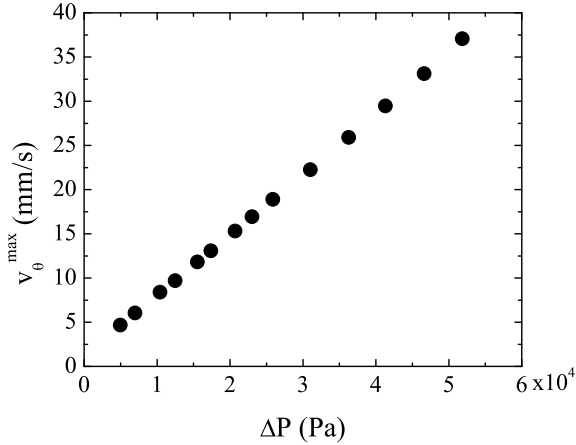


Figure 3: Maximum of the velocity profile versus pressure drop along the channel ΔP for the solvent of water with 65% of sucrose in a laminar channel flow.

the wall. Due to curvature in serpentine geometry of the channel, the profiles of the longitudinal velocity are not symmetric relatively to the middle plane in contrast to a straight channel. Figure 3 shows a linear dependence of the maximum values of the velocity profiles V_{θ}^{max} (or the discharge) in a laminar flow of the solvent as a function of the pressure drop ΔP along the channel, which is used for calibration.

As a working fluid, a 65% sucrose-water solvent with addition of 1% NaCl, 250 ppm of NaN_3 , and 80 ppm by weight high molecular weight polyacrylamide (PAAm) ($M_w = 18$ Mda, supplied by Polysciences), was used. It was prepared from a master water solution contained 3000 ppm of PAAm, 1% NaCl, 250 ppm of NaN_3 , and 3% of iso-propanol [14]. The viscosity of the solvent

$\eta_s = 113.8 \text{ mPa} \cdot \text{s}$ and the polymer solution $\eta = 137.6 \text{ mPa} \cdot \text{s}$ were measured at 22 ± 0.5 °C, the same temperature kept during the experiment. The longest polymer relaxation time measured by the stress relaxation method was $\lambda = 11.5$ sec and was found to be independent of the shear rate [15] (it differs from values used in Ref. [5, 13], where the polymer relaxation time was measured by the small amplitude oscillation method). The solution density was $\rho = 1.303 \pm 0.03 \text{ g cm}^{-3}$. The inflow of a polymer solution into the channel was generated via two inlets by a compressed nitrogen gas at pressures between 0.35 and 8.5 psi depending on Wi . The gas pressure was regulated and measured via a regulated pressure gauge with a precision of ± 5 Pa. The compressed gas was fed into two plastic cylinders containing a working polymer solution. The cylinders were connected to the channel inlets by Tygon tubes with inner diameter of 1.0 mm, sufficiently large to prevent a possibility of an elastic instability already in the tubes. The Weissenberg numbers $Wi = (2V_{\theta}^{max}/d)\lambda$ reached in the experiment by a such arrangement were in the range from 0 to 950. The maximum $Re = V_{\theta}^{max}d\rho/\eta$ was ~ 0.54 , so that the inertial effects in the flow were negligible, as was already shown in the earlier experiments [3–5, 13].

III. PROPERTIES OF ELASTIC TURBULENCE

A. Flow structure and experimental determination of the elastic instability threshold

We searched experimentally for the onset of the elastic instability in our channel with the aspect ratio $d/R_i = 1$. In order to figure out the range of the elastic turbulence region, we plot the values of $\langle V_{\theta} \rangle$ at $r/d = 0.5$ and V_{θ}^{rms} as a function of Wi in Figs. 4 and 5. From the both plots one concludes that the elastic instability onset corresponds to the change in the slope that occurs at $Wi_c \simeq 200$ on the both plots. Similar change in the slope takes place in the dependence of V_r^{rms} on Wi at about the same value of Wi_c though the data is noisier (Fig. 6). An additional change in functional behavior of V_{θ}^{rms} and V_r^{rms} versus Wi occurs at $Wi \approx 350 - 400$, where the transition region to elastic turbulence is ended. In all three plots in Figures 4, 5, and 6 the arrows indicate the onset of the elastic instability and the end of the transitional region towards elastic turbulence. Thus, the range of developed elastic turbulence can be considered for Wi from about 350 up to 950.

Using the results of the PIV measurements one calculates the various components of velocity gradient field as a function of r at different values of Wi . Figure 7 presents the data for $Wi_{loc} \equiv (\partial V_{\theta}/\partial r)_{rms}\lambda$ versus Wi averaged over r/d from 0.2 till 0.5 in the bulk flow. In the range of elastic turbulence for Wi from 350 till 950 the data in log-linear presentation in Fig. 7 are fitted by a linear fit, so $Wi_{loc} = 82.2 \exp(Wi/919.2)$. Figure 8 show $(\partial V_r/\partial r)^{rms}$ averaged over r/d from 0.2 till 0.5 in the

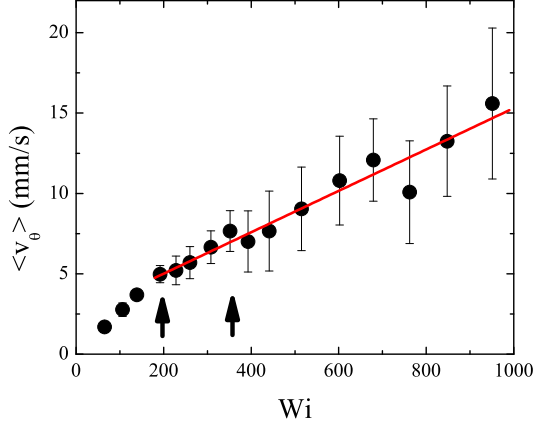


Figure 4: The mean longitudinal velocity at $r/d = 0.5$ as a function of Wi . Arrows indicate the elastic instability onset and the ending of a transitional regime to elastic turbulence, respectively.

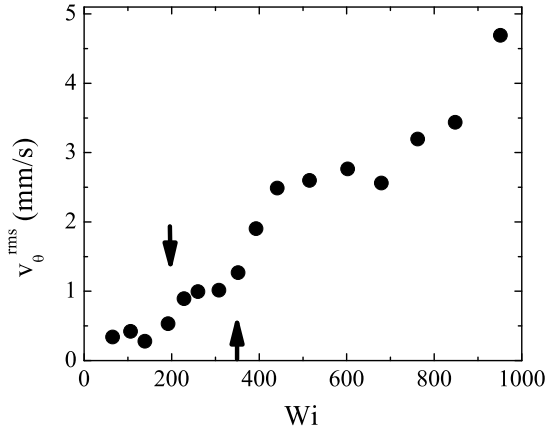


Figure 5: Root mean square of the longitudinal velocity V_θ^{rms} versus Wi . Arrows indicate the elastic instability onset and the ending of a transitional regime to elastic turbulence, respectively.

bulk flow region as a function of Wi . Here the data can be also fitted linearly by $(\partial V_r / \partial r)^{rms} = 5.64 + 0.055Wi$ in the elastic turbulence range. All PIV data were averaged over 1000 velocity fields to get both average velocity and its rms values as well as the velocity gradient components.

B. Velocity and velocity gradient profiles and the boundary layer problem

As it is demonstrated above, a channel flow of a polymer solution at sufficiently large Wi above the elastic

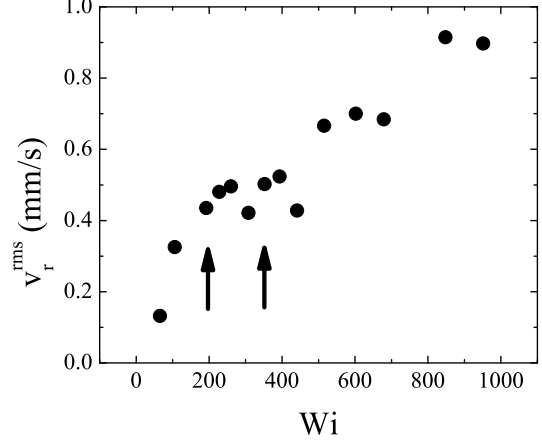


Figure 6: Root mean square of the transversal velocity V_r^{rms} versus Wi . Arrows indicate the elastic instability onset and the ending of a transitional regime to elastic turbulence, respectively.

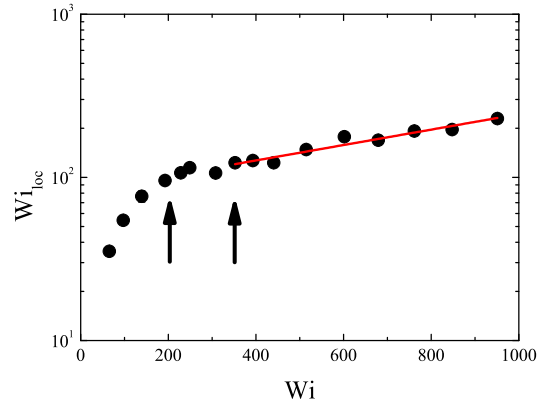


Figure 7: The local Weissenberg number $Wi_{loc} = (\partial V_\theta / \partial r)^{rms} \lambda$ averaged over r/d from 0.2 till 0.5 as a function of Wi . Arrows indicate the elastic instability onset and the ending of a transitional regime to elastic turbulence, respectively.

instability threshold Wi_c is chaotic with large velocity fluctuations. Figure 9 shows the profiles of the average longitudinal velocity $\langle V_\theta \rangle(r/d)$ across the channel for various values of Wi from below the elastic instability and up to the highest values. A boundary layer characterized by a sharp drop of $\langle V_\theta \rangle(r/d)$ at about $r/d \leq 0.05$ is clearly seen at Wi above 192. A full profile of $\langle V_\theta \rangle(r/d)$ across the channel at $Wi = 951$ is presented in Fig. 10, where both boundary layers are clearly identified.

From the same velocity measurements the profiles of the average transversal velocity $\langle V_r \rangle$, and the rms fluctuations of the longitudinal V_θ^{rms} and transversal V_r^{rms} components of the velocity for various Wi are also ob-

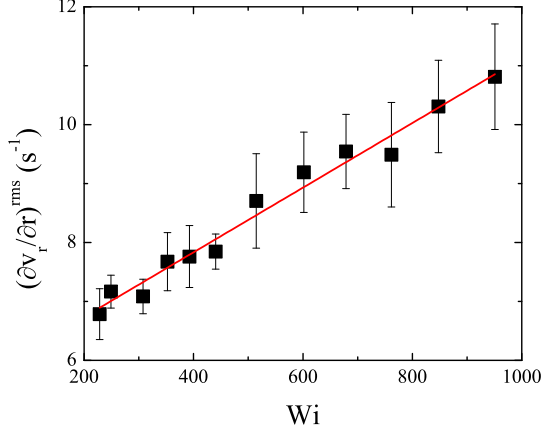


Figure 8: $(\partial V_r / \partial r)^{rms}$ averaged over r/d from 0.2 till 0.5 versus Wi . Solid line is a linear fit to the data $(\partial V_r / \partial r)^{rms} = (5.64 \pm 0.15) + (0.055 \pm 0.002)Wi$ in the elastic turbulence regime from $Wi = 350$ till 950.

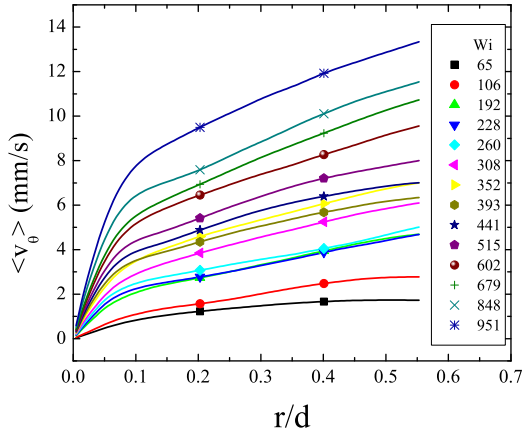


Figure 9: Mean longitudinal velocity profiles across the channel of a polymer solution flow for various Wi (starting from small values at bottom to top; $r = 0$ corresponds to the inner channel wall).

tained (see Figs. 11,12,13).

First, by comparing Figs. 9 and 11 one finds that $\langle V_r \rangle$ is close to zero in the limit of error bars across the channel and $\langle V_\theta \rangle$ exceeds it by more than two orders of magnitude. Whereas rms fluctuations of the longitudinal and transversal components are of the same order of magnitude that follows from Figs. 12 and 13. Figure 14 shows $(\partial V_\theta / \partial r)^{rms}$ versus r/d at various Wi in the whole range of its variation. Analogously, the component $(\partial V_r / \partial r)^{rms}$ as a function of r/d is plotted for various Wi in Fig. 15. As before, all PIV data were averaged over 1000 velocity fields to get both average velocity and its rms values as well as the velocity gradient

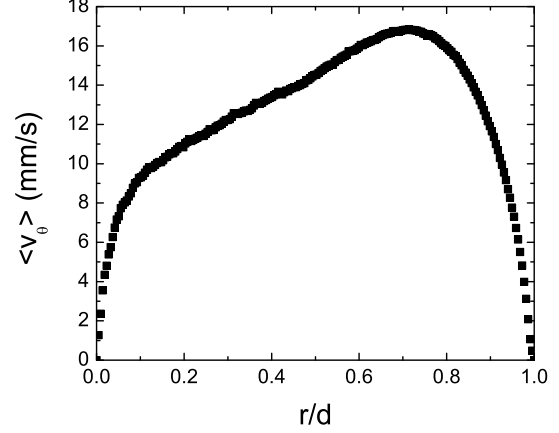


Figure 10: The entire mean longitudinal velocity profile across the channel of a polymer solution flow for $Wi = 951$.

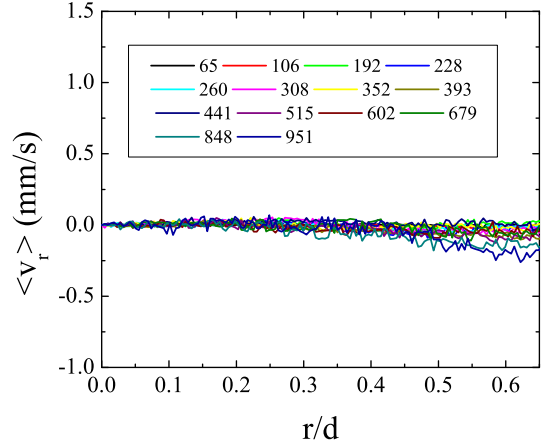


Figure 11: Mean transversal velocity profiles across the channel of a polymer solution flow for various Wi .

components.

Second, we present in Figs. 16, 17 time dependencies of $V_\theta(t)$ and $V_r(t)$ for fixed value of $r/d = 0.5$ in the bulk flow at several values of Wi and on time interval much larger than λ . In the elastic turbulence regime at $Wi > 350$ strong fluctuations in the both components of the velocity are observed.

Clearly identified boundary layer regions near the wall in the both average velocity and rms of fluctuations of both components of the velocity and velocity gradient profiles across the channel in Figs. 9,10,14,15 can be better study after subtraction from each velocity profile a linear part of the profile found in the bulk region with the slope $d\langle V_\theta \rangle / dr$ (see Figs. 9 and 10) and then scaling its value to unity. As the result, all longitudinal velocity profiles at Wi in the range of elastic turbulence above 350 collapse on a single curve demonstrating independence

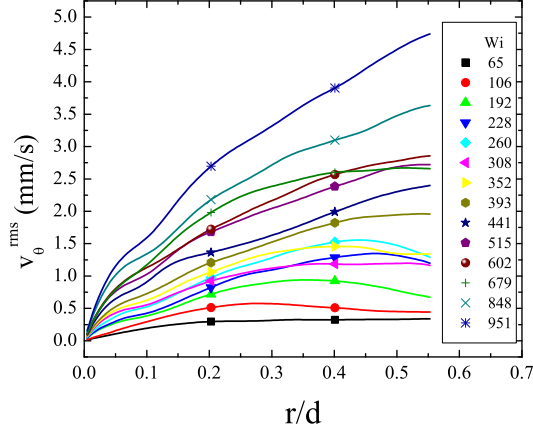


Figure 12: RMS fluctuations of the longitudinal velocity profiles across the channel of a polymer solution flow for various Wi (starting from small values at bottom to top; $r = 0$ corresponds to the inner channel wall).

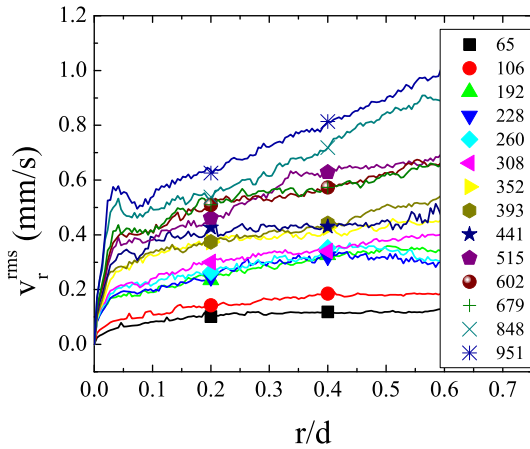


Figure 13: Rms fluctuations of transversal velocity profiles across the channel of a polymer solution flow for various Wi (starting from small values at bottom to top; $r = 0$ corresponds to the inner channel wall).

of the boundary layer width on Wi (Figs. 18,19). This property of the boundary layer agrees with that observed in the swirling flow [7]. The boundary layer width is also independent of Wi_{loc} (Fig. 19, inset).

And finally, we present in Fig. 20 the dependencies of $(\partial V_\theta / \partial r)^{rms}$ in the bulk and in the boundary layer regions as a function of Wi taken from the plots in Figs. 7 and 14. The peak values of $(\partial V_\theta / \partial r)^{rms}$ in the boundary layer exceed those in the bulk up to two times only compared to at least an order of magnitude in the swirling flow [7, 22], probably due to the limiting spatial resolution of micro-PIV. The latter smears out the peak value of $(\partial V_\theta / \partial r)^{rms}$.

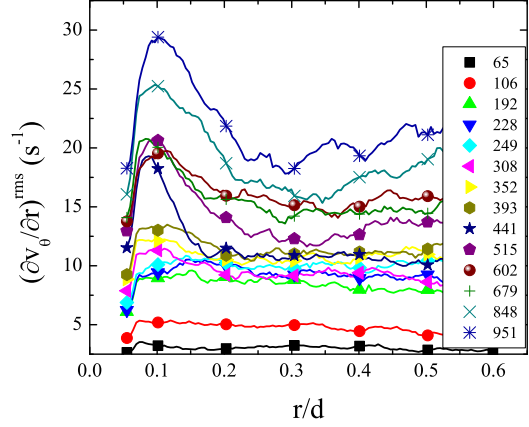


Figure 14: $(\partial V_\theta / \partial r)^{rms}$ versus r/d for various Wi from bottom to top.

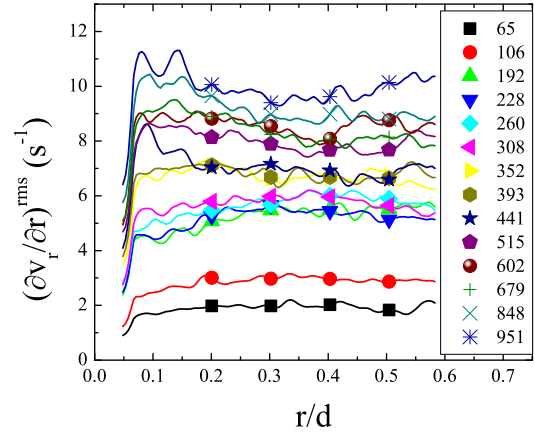


Figure 15: $(\partial V_r / \partial r)^{rms}$ versus r/d for various Wi from bottom to top.

C. Temporal and spatial correlation functions of both velocity components and their gradients.

We studied both temporal and spatial (across the channel) correlation functions of the both velocity components. Figure 21 shows temporal correlation functions of the longitudinal and transversal velocity components $C(\tau) = \langle \delta V(\tau) \delta V(0) \rangle / \langle (\delta V(0))^2 \rangle$, where $\delta V_\theta(\tau) \equiv V_\theta(\tau) - \langle V_\theta \rangle$, and $\delta V_r(\tau) \equiv V_r(\tau) - \langle V_r \rangle$ at several Wi values in the elastic turbulence regime taken at the bend $N = 42$. The corresponding correlation time calculated as $\tau_{corr} = \int t C_\tau(t) dt / \int C_\tau(t) dt$ for the both velocity components as a function of Wi are presented in Fig. 22. As can be seen in Fig. 22, the correlation time for $\delta V_\theta(\tau)$ is considerably larger than for $\delta V_r(\tau)$.

The spatial correlation functions $C(r/d) = \langle \delta V(r/d) \delta V(0) \rangle / \langle (\delta V(0))^2 \rangle$ and the corresponding

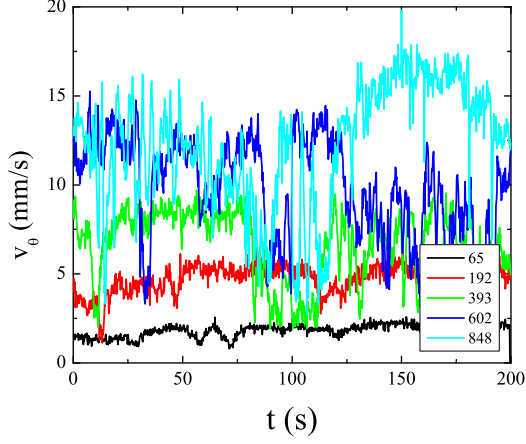


Figure 16: Time series of the longitudinal velocity at $r/d = 0.5$ for various Wi .

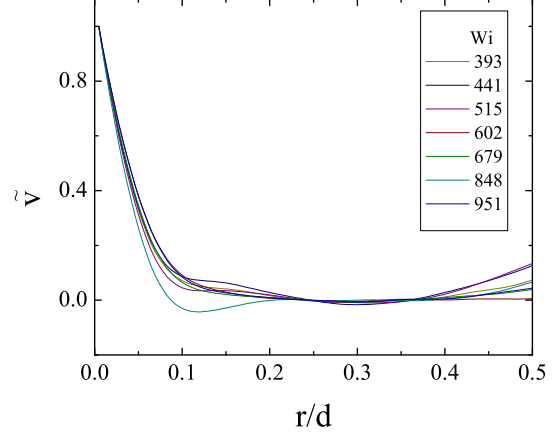


Figure 18: Normalized and scaled down $\langle \tilde{V}_\theta \rangle(r/d)$ velocity profiles at various Wi .

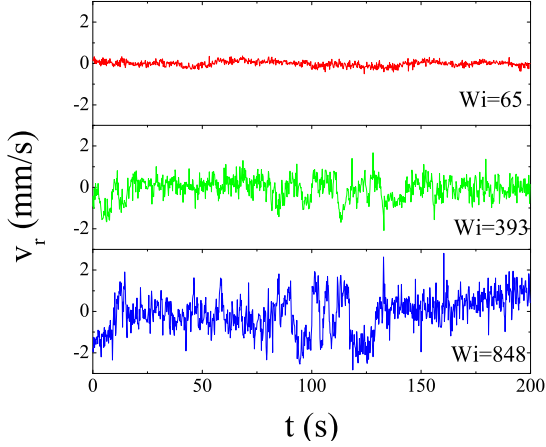


Figure 17: Time series of the transversal velocity at $r/d = 0.5$ for various Wi .

correlation lengths for the both velocity components calculated as $l_{corr}/d = \int (r/d) C(r/d) dr/d / \int C(r/d) dr/d$ are shown for several Wi in Figs. 23 and 24. Here $\delta V_\theta(r/d) \equiv V_\theta(r/d) - \langle V_\theta \rangle$ and $\delta V_r(r/d) \equiv V_r(r/d) - \langle V_r \rangle$. The correlation lengths for both components are rather close and independent of Wi . Using the Taylor hypothesis one can compare the correlation lengths along the flow with those across the flow. As follows from the data in Fig. 22, the correlation time for the longitudinal component of velocity is about $\tau_{corr}/\lambda \simeq 4$ that gives for, let say, $Wi = 600$ the correlation length along the flow $\Gamma/d = \tau_{corr} \langle V_\theta \rangle \simeq 370$ that is about 2000 times larger than l_{corr}/d . Similarly, the correlation functions $\tilde{C}_\theta(r/d)$ and $\tilde{C}_r(r/d)$ as well as the corresponding correlation lengths $l_{\theta,corr}/d$ and $l_{r,corr}/d$ of the both velocity gradients $\partial V_\theta/\partial r$ and $\partial V_r/\partial r$ are also calculated, and the results for different Wi were presented in Figs. 25

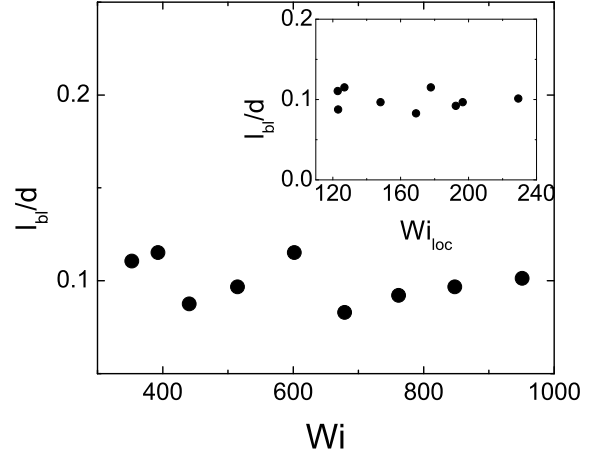


Figure 19: Velocity boundary layer width l_{bl} versus Wi . Inset: Velocity boundary layer width l_{bl} versus Wi_{loc} .

and 26. First, the correlation functions have minimum at $r/d \approx 0.06$, and second, the correlation lengths are up to an order of magnitude shorter than for the velocities (see Fig. 26 versus Fig. 24) and grow with Wi .

D. Statistics of velocity gradients and their structure functions.

Further verification of the scaling laws in elastic turbulence in the channel flow comes from the statistical analysis of the velocity field. We point out that the statistical analysis of the longitudinal velocity component in spatial and in particular temporal domains show large scatter due to insufficient data that makes the analysis unreliable. On the other hand, the same analysis in a

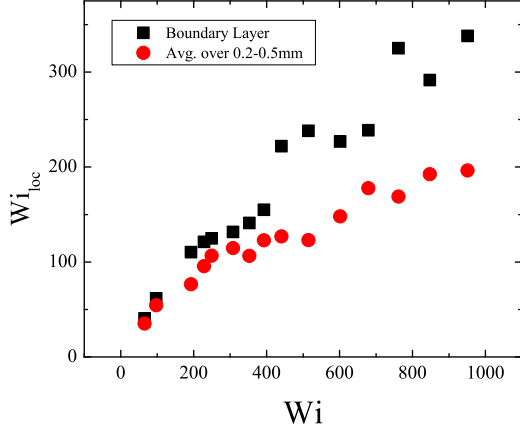


Figure 20: The peak values of $(\partial V_\theta / \partial r)^{rms}$ in the bulk and boundary layer versus Wi .

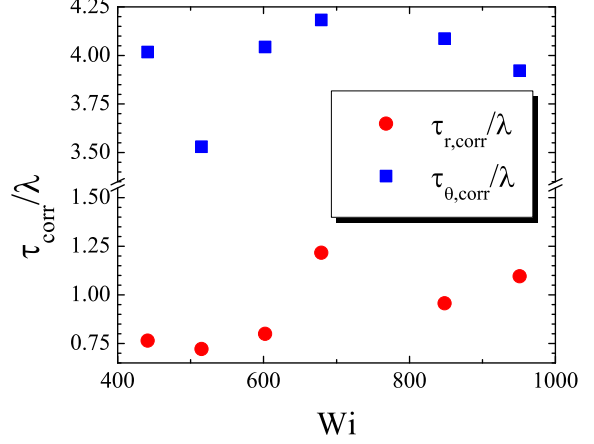


Figure 22: Normalized correlation times $\tau_{\theta,corr}/\lambda$ and $\tau_{r,corr}/\lambda$ versus Wi for both V_θ and V_r , respectively.

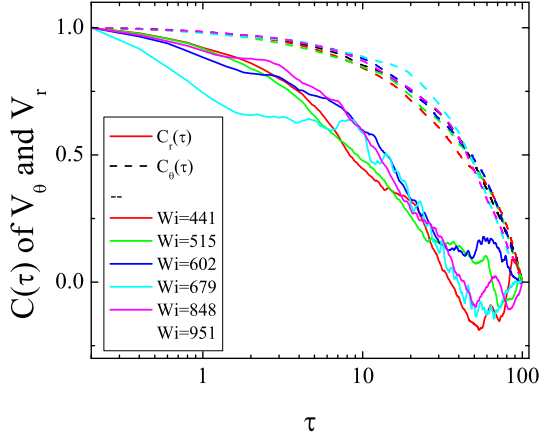


Figure 21: Temporal correlation functions $C_\theta(\tau)$ of $V_\theta(t)$ and temporal correlation functions $C_r(\tau)$ of $V_r(t)$, respectively, at several Wi above Wi_c taken at the bend $N = 42$.

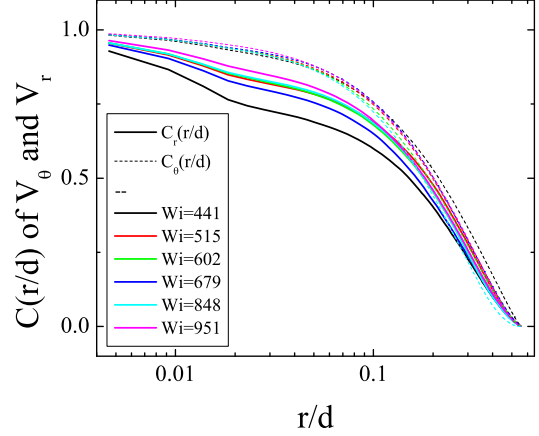


Figure 23: Spatial correlation functions $C_\theta(r/d)$ of $V_\theta(r/d)$ and spatial correlation functions $C_r(r/d)$ of $V_r(r/d)$, respectively, at several Wi above Wi_c taken at the bend $N = 42$.

spatial domain of both components of the velocity gradients exhibits much better results.

First, we conducted the statistical analysis of the spatial increments of the radial gradients of the longitudinal velocity $\delta \partial V_\theta / \partial r(\delta r/d) = [\partial V_\theta / \partial r(r/d + \delta r/d) - \partial V_\theta / \partial r(r/d)] / \delta \partial V_\theta / \partial r(\delta r/d)_{rms}$ in a wide range of the spatial scales from 9.2 to 46 μm with the step 4.6 μm at $Wi = 951$ for the bend $N = 42$. The corresponding PDFs of the spatial increments of the normalized longitudinal velocity gradients $\delta(\partial V_\theta / \partial r)(\delta r/d)$ have a small Gaussian cap and show well-pronounced exponential tails, clear scale invariance and symmetry with small scatter in spite of low statistics (see Fig. 27). Further analysis can be done in equivalent way either by direct calculations of the structure functions or by calculations

of the moments of PDFs. The corresponding second moments of PDFs $S_{2,\theta}(\delta r/d)$ on $\delta r/d$ in log-log coordinates for several values of Wi show the scaling region in $\delta r/d$ between 0.01 and 0.05 in Fig. 28. The structure functions of the higher even orders up to $p = 8$ $S_{p,\theta}(\delta r/d)$ as a function of $\delta r/d$ are plotted in log-log coordinates at $Wi = 951$ in Fig. 29. Due to symmetrical shape of PDFs odd moments are zero. The power dependence of the structure functions (or moments) $S_{p,\theta}(\delta r/d) \sim (\delta r/d)^{\zeta_{p,\theta}}$ is found in the range of $\delta r/d$ between 0.004 and 0.05. The plot in Fig. 30 demonstrates independence of the scaling exponents $\zeta_{2,\theta}$ and $\zeta_{4,\theta}$ of Wi in the whole range of elastic turbulence. The dependence of $\zeta_{p,\theta}$ which are surprisingly close to the linear scaling with $\zeta_{p,\theta} = 0.75p$ (see Fig. 31). The latter is very different from passive scalar behavior [14]. Analogous analysis was conducted

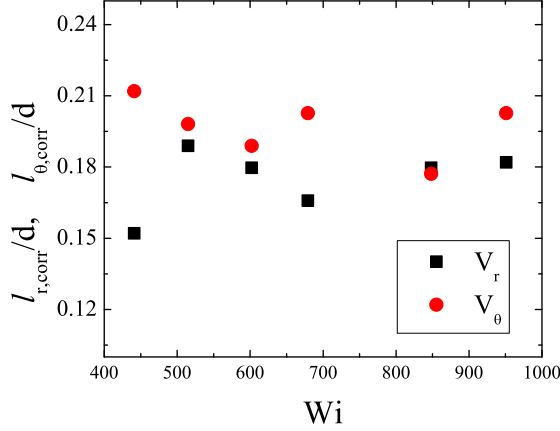


Figure 24: Normalized correlation length $l_{\theta,corr}/d$ and $l_{r,corr}/d$ versus Wi for both V_{θ} and V_r , respectively.

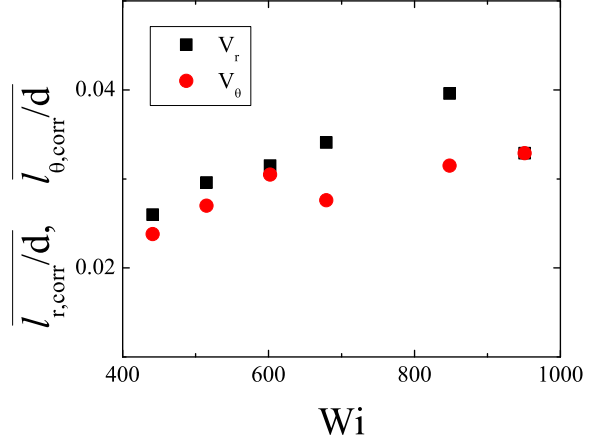


Figure 26: Normalized correlation length $\tilde{l}_{\theta,corr}/d$ and $\tilde{l}_{r,corr}/d$ versus Wi for both $\partial V_{\theta}/\partial r$ and $\partial V_r/\partial r$, respectively.

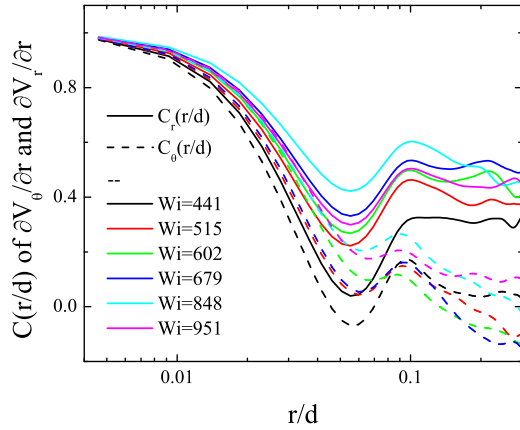


Figure 25: Spatial correlation functions $\tilde{C}_{\theta}(r/d)$ of $\partial V_{\theta}/\partial r$ and spatial correlation functions $\tilde{C}_r(r/d)$ of $\partial V_r/\partial r$, respectively, at several Wi above Wi_c taken at the bend $N = 42$.

also for the radial gradients of the transversal velocity $\delta(\partial V_r/\partial r)(\delta r/d)$ and the obtained results were very similar to the velocity gradient of the longitudinal component. The corresponding PDFs also exhibit similar features: small Gaussian cap, exponential tails though not so clean, scale invariance and symmetry (see Fig. 32). As the result, the second $S_{2,r}(\delta r/d)$ and higher order even $S_{p,r}(\delta r/d)$ moments (or structure functions) up to $p = 8$ show scaling in the same range of scales (Figs. 33, 34, 35) with the scaling exponents $\zeta_{p,r}$ and Wi (see Fig. 35) and p (see Fig. 36) dependence close to those found for $\delta(\partial V_{\theta}/\partial r)(\delta r/d)$.

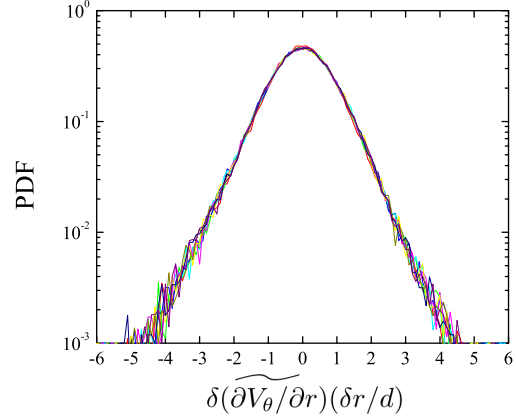


Figure 27: PDFs of the spatial increments of the normalized longitudinal velocity radial gradient $\delta(\partial V_{\theta}/\partial r)(\delta r/d) = [\partial V_{\theta}/\partial r(r/d + \delta r/d) - \partial V_{\theta}/\partial r(r/d)]/\delta(\partial V_{\theta}/\partial r)(\delta r/d)_{rms}$ at different length scales (from 9.2 to 46 μm with the step 4.6 μm) at $Wi = 951$ based on its spatial velocity field measurements for the bend $N = 42$.

IV. DISCUSSION

Let us summarize first the main observations reported above.

(i) Well-defined threshold of the elastic instability in a curvilinear channel flow is identified by the average longitudinal velocity and rms longitudinal and transversal velocity fluctuations (Figs. 4-6). The transition to elastic turbulence regime is determined from V_{θ}^{rms} and V_r^{rms} as well as $(\partial V_{\theta}/\partial r)^{rms}$, or Wi_{loc} , dependencies on Wi (Figs. 5-7). In the latter case, an exponential dependence of Wi_{loc} on Wi above the transition to elastic turbulence is observed (Fig. 7). (ii) The profiles of the average longitudinal velocity are altered drastically in

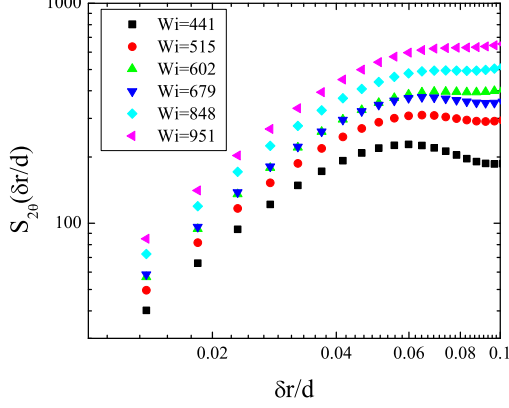


Figure 28: Second moments $S_{2,\theta}(\delta r/d)$ of PDFs of the longitudinal velocity gradient increments $\delta(\partial V_\theta/\partial r(\delta r/d))$ versus $\delta r/d$ for several values of Wi (in log-log coordinates).

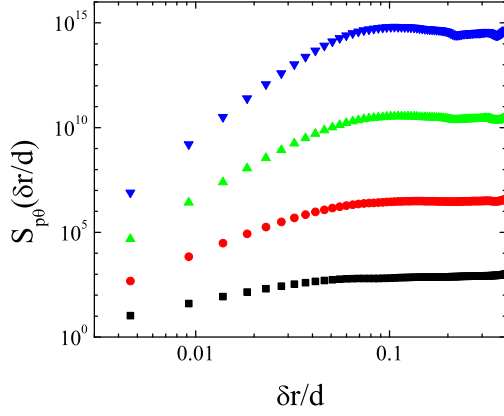


Figure 29: Structure functions $S_{p,\theta}(\delta r/d)$ of the longitudinal velocity gradient spatial increments $\delta(\partial V_\theta/\partial r(\delta r/d))$ up to $p = 8$ (only even) for $Wi = 951$ (in log-log coordinates).

elastic turbulence compared to a laminar flow (Fig. 9). In the elastic turbulence regime the characteristic boundary layer is clearly identified near the wall (Fig. 9 and 10). Being normalized and rescaled, all velocity profiles are collapsed on one curve with a horizontal flat part in the bulk and sharp change near the wall, so that all profiles have the same boundary layer width independent of Wi (Figs. 18 and 19). (iii) On the other hand, a profile of $(\partial V_\theta/\partial r)^{rms}$ (Fig. 14) shows a peak much closer to the wall, inside the velocity boundary layer discussed above, which location near the channel wall is also independent of Wi . As we discussed in our early papers on elastic turbulence in a swirling flow [6, 7], the peak in $(\partial V_\theta/\partial r)^{rms}$ means also the maximum in elastic stresses, and so the boundary layer is defined by the non-uniform spatial distribution of the elastic stresses across the channel. (iv)

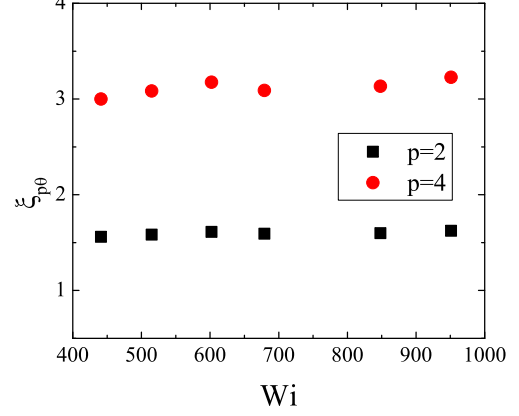


Figure 30: Scaling exponents of the second $S_{2,\theta}(\delta r/d)$ and fourth $S_{4,\theta}(\delta r/d)$ moments of the longitudinal velocity gradient increments $\delta(\partial V_\theta/\partial r(\delta r/d))$ for various Wi .

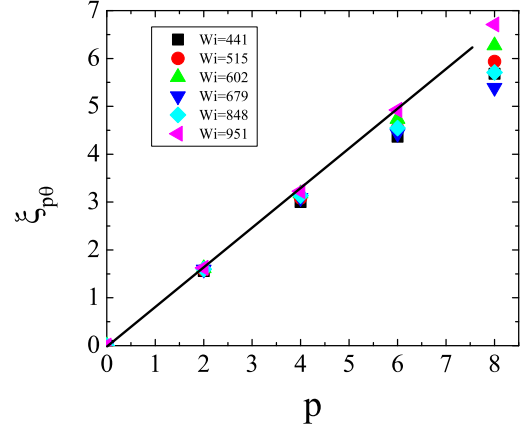


Figure 31: Scaling exponents $\zeta_{p,\theta}$ of the structure functions of the longitudinal velocity gradients spatial increments $\delta(\partial V_\theta/\partial r(\delta r/d))$ versus p for various Wi .

The correlation times determined from the temporal correlation functions for both velocity components differ up to 5 times. The correlation time for the transversal velocity component $\tau_{r,corr}$ is of the order of the polymer relaxation time, whereas the correlation time of the longitudinal velocity component $\tau_{\theta,corr}$ is several times larger (Figs. 21 and 22). (v) The correlation lengths found from the spatial correlation functions of both velocity components are of about $l_{corr}/d \approx 0.18$ for both velocity components in the elastic turbulence regime (Figs. 23 and 24). On the other hand, the correlation lengths obtained from the spatial correlation functions of the radial gradients of the longitudinal and transversal velocity components are about 6 times smaller than for the velocity components in the whole range of elastic turbulence (Figs. 25 and 26). (vi) PDFs of the spatial increments

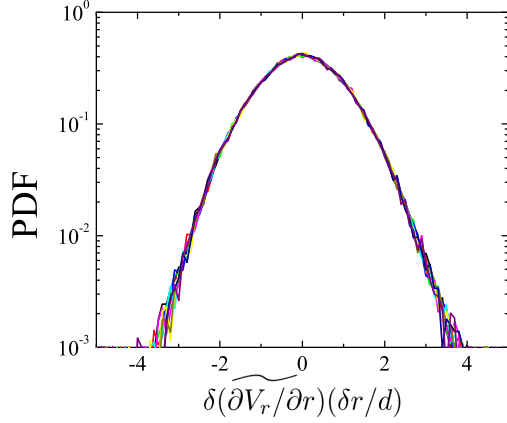


Figure 32: PDFs of the spatial increments of the normalized transversal velocity radial gradient $\delta(\partial V_r / \partial r)(\delta r/d) = [\partial V_r / \partial r(r/d + \delta r/d) - \partial V_r / \partial r(r/d)] / \delta(\partial V_r / \partial r)(\delta r/d)_{rms}$ at different length scales from 9.2 to 46 μm with the step 4.6 μm at $Wi = 951$ based on its spatial velocity field measurements for the bend $N = 42$.

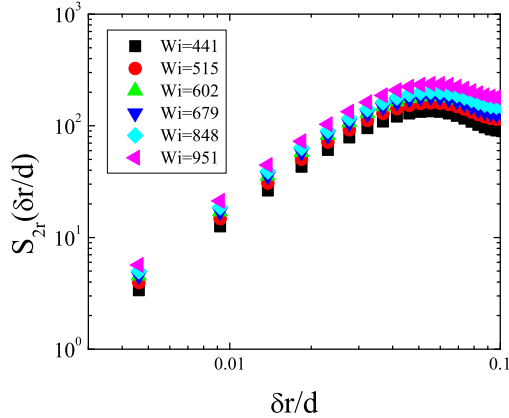


Figure 33: Second moments $S_{2,r}(\delta r/d)$ of PDFs of the transversal velocity gradient increments $\delta(\partial V_r / \partial r)(\delta r/d)$ versus $\delta r/d$ for several values of Wi (in log-log coordinates).

of the radial gradients of the longitudinal and transversal velocity components in a wide range of the length scales up to the boundary layer width demonstrate the scale invariance and exponential tails. It reminds very much the properties of the PDFs of passive scalar in the Batchelor regime [14]. On the other hand, the second and higher order even moments of the PDFs, contrary to the passive scalar logarithmic dependence on spatial scales, show an algebraic increase with spatial increment with the scaling exponents $\zeta_{p,\theta}$ and $\zeta_{p,r}$, which dependence on p mildly deviates from linear dependence.

There are several important messages, which follow from the observations summarized above. (i) The elastic instability transition in a curvilinear channel is continu-

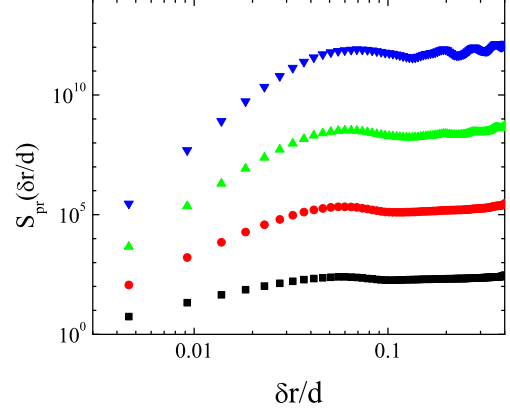


Figure 34: Structure functions $S_{p,r}(r/d)$ of the transversal velocity gradient increments $\delta(\partial V_r / \partial r)(\delta r/d)$ up to $p = 6$ (only even) for $Wi = 951$ (in log-log coordinates).

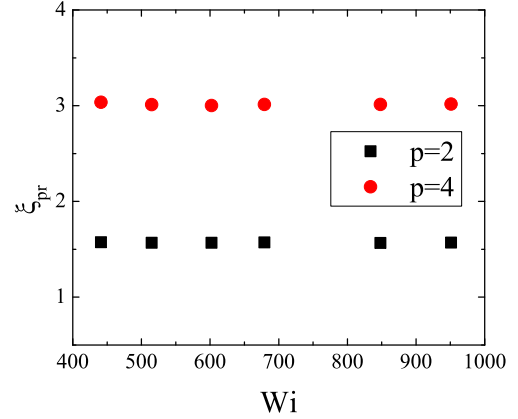


Figure 35: Scaling exponents of the second $S_{2,r}(\delta r/d)$ and fourth $S_{4,r}(\delta r/d)$ moments of the transversal velocity gradient increments $\delta(\partial V_r / \partial r)(\delta r/d)$ for various Wi .

ous one (forward bifurcation) as already found in early experiments [4, 5, 13], in contrast to those observed in Couette-Taylor flow [4] and swirling flow between two disks [4, 7]. (ii) Contrary to the predictions, Wi_{loc} grows with Wi in the elastic turbulence regime and its value exceeds the theoretically predicted an order of unity by more than two orders of magnitude. (iii) The profiles of the average longitudinal component of the velocity reveal the boundary layer, which width is independent of Wi in the whole range of elastic turbulence and being scaled by the channel width also independent on the characteristic size of the system. Both existence of the boundary layer and independence of its width on the control parameters of the flow are rather surprising features, in particular taking into account that the largest scale of the flow is smaller than the dissipation scale. This fact was already

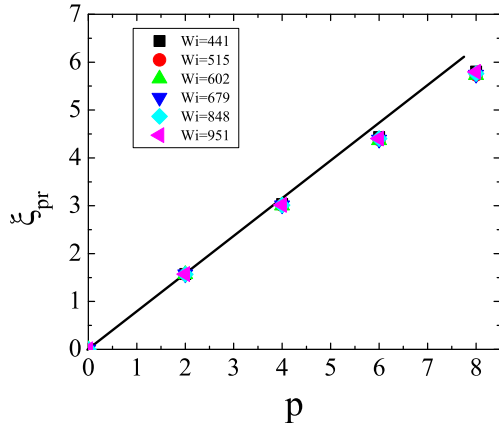


Figure 36: Scaling exponents $\zeta_{p,r}$ of the structure functions of the transversal velocity gradients increments $\delta(\partial V_r/\partial r(\delta r/d))$ versus p for various Wi .

reported in Refs. [6, 7] for the swirling flow. (iv) The boundary layer observed in the average velocity profiles is a reflection of a nonuniform distribution of the rms of the radial gradient of the longitudinal velocity. Indeed, the latter profiles exhibit more intricate behavior with sharp peaks inside the velocity boundary layer, which locations are independent of Wi but the peak values grow with Wi . Since $(\partial V_\theta/\partial r)^{rms}$ controls the degree of polymer stretching in a random flow and in this way the elastic stress, one concludes that similar nonuniform distribution of the elastic stress can be expected near the wall in elastic turbulence. It is a subject for future experiments. The expected nonuniform distribution of the elastic stress reminds a nonuniform distribution of passive scalar in a bounded channel flow [13, 14, 23] with rare and strong ejection of jets occurring in the diffusion boundary layer and protruding into the peripheral region and even further into the bulk of the channel flow [14, 24, 25]. These jets are considerably alter mixing significantly reducing its efficiency. One can expect an emergence of similar jets of the elastic stresses, concentrated near the wall in the boundary layer, and ejected into the bulk. In such a way the elastic stresses are introduced into the flow. (v) Another characteristic spatial scale in the flow is the correlation length of the velocity field l_{corr} , which is about

twice larger than the velocity boundary layer l_{bl} . Since elastic turbulence is a smooth random flow, where only a few large scale modes dominate the dynamics, one expects that l_{corr} should be of the order of d . On the other hand, the correlation length defined from the correlation function of the velocity gradients \tilde{l}_{corr} is about an order of magnitude smaller than l_{corr} . This fact points out on the relation of \tilde{l}_{corr} with the characteristic spatial scale corresponding to the peak location of $(\partial V_\theta/\partial r)^{rms}$ near the wall inside the velocity boundary layer width. Then due to eruption of jets of elastic stresses this characteristic scale is observed in the bulk. (vi) The same range of spatial scales are found in the scaling region of the structure functions of the velocity gradients S_p that once more indicates a possible influence of jets protruding into the bulk of the flow.

V. CONCLUSIONS

To conclude, the experimental results show that one of the main predictions of the theory of elastic turbulence, namely the saturation of Wi_{loc} in the bulk flow of elastic turbulence contradicts to the experimental observations both qualitatively and quantitatively in spite of the fact that the theory explains well the observed sharp decay of the velocity power spectrum [9, 17]. The nonuniform distribution of $(\partial V_\theta/\partial r)^{rms}$ across the channel points out on the nonuniform distribution of elastic stresses. The latter may lead to the rare and strong eruption of the jets of elastic stresses from boundary layer into the bulk and in this way to introduce small spatial scales into the bulk flow. The existence of the resulting velocity boundary layer width and its peculiar properties require a proper theoretical description. Thus the experimental findings call for further development of theory of elastic turbulence in a bounded container, similar to what was done for a passive scalar problem [23].

Acknowledgments

This work is supported by grants from Israel Science Foundation and Lower Saxony Ministry of Science and Culture Cooperation Grant.

-
- [1] R. B. Bird et al. *Dynamics of Polymer Liquids*, (Wiley, New York, 1987).
 - [2] A. Groisman and V. Steinberg, *Nature* **405**, 53 (2000).
 - [3] A. Groisman and V. Steinberg, *Nature* **410**, 905 (2001).
 - [4] A. Groisman and V. Steinberg, *New J. Phys.* **6**, 29 (2004).
 - [5] T. Burghelea, E. Segre, I. Bar-Joseph, A. Groisman, V. Steinberg, *Phys. Rev. E* **69** 066305 (2004).
 - [6] T. Burghelea, E. Segre, V. Steinberg, *Phys. Rev. Lett.* **96**, 214502 (2006).
 - [7] T. Burghelea, E. Segre, V. Steinberg, *Phys. Fluids* **19**, 053104 (2007).
 - [8] Y. Jun and V. Steinberg, *Phys. Rev. Lett.* **102**, 124503 (2009).
 - [9] A. Fouxon, V. Lebedev, *Phys. Fluids* **15**, 2060 (2003).
 - [10] S. Berti, A. Bistagnino, G. Boffetta, A. Celani, S. Musacchio, *Phys. Rev. E* **77**, 055306(r) (2008).
 - [11] S. Berti and G. Boffetta, *Phys. Rev. E* **82**, 036314 (2010).
 - [12] H. Yatou, *Phys. Rev. E* **82**, 036310 (2010).

- [13] T. Burghlea, E. Segre, and V. Steinberg, *Phys. Rev. Lett.* **92**, 164501 (2004).
- [14] Y. Jun and V. Steinberg, *Phys. Fluids* **22**, 123101 (2010).
- [15] Y. Liu, Y. Jun, V. Steinberg, *J. Rheology* **53**, 1069 (2009).
- [16] G. K. Batchelor, *J. Fluid Mech* **5**, 113 (1959).
- [17] E. Balkovsky, A. Fouxon, V. Lebedev, *Phys. Rev. E* **64**, 056301 (2001).
- [18] E. Balkovsky, A. Fouxon, V. Lebedev, *Phys. Rev. Lett.* **84**, 4765 (2000).
- [19] M. Chertkov, *Phys. Rev. Lett.* **84**, 4761 (2000).
- [20] S. Gerashchenko, C. Chevillard, V. Steinberg, *Europhys. Lett.* **71**, 221 (2005).
- [21] Y. Liu and V. Steinberg, *Europhys. Lett.* **90**, 44002 (2010).
- [22] Y. Jun and V. Steinberg, to be published
- [23] M. Chertkov and V. Lebedev, *Phys. Rev. Lett.* **90**, 034501 (2003).
- [24] A. Chernykh and V. Lebedev, *JETP Lett.* **87**, 682 (2008).
- [25] H. Salman, P. H. Haynes, *Phys. Fluids* **19**, 067101 (2007).